

# Spin caloritronics in spin semiconducting armchair graphene nanoribbons

Majid Shirdel-Havar and Rouhollah Farghadan\*

Department of Physics, University of Kashan, Kashan 87317-53153, Iran



(Received 2 February 2018; revised manuscript received 30 April 2018; published 13 June 2018)

We designed a spin-caloritronics device based on armchair graphene nanoribbons (AGNRs). We theoretically show that a trapezoidal-shaped graphene flake consisting of four zigzag edges bridged between two AGNRs becomes a spin semiconductor with a tunable spin-dependent transmission gap. The results indicate that the appearance of spin semiconducting properties with spin-dependent localized transmission peaks around the Fermi level could produce the spin-caloritronics effects of AGNRs. Interestingly, the values of the spin Seebeck coefficient  $S_S$  are comparable to values obtained for zigzag graphene nanoribbons, and also  $S_S$  sensitively increases as the transmission gap increases. Furthermore, by engineering the position and orientation of a triangular antidot only in the scattering region, both  $S_S$  and the spin figure of merit could be separately enhanced at room temperature.

DOI: [10.1103/PhysRevB.97.235421](https://doi.org/10.1103/PhysRevB.97.235421)

## I. INTRODUCTION

The combination of spintronics [1,2] and thermoelectricity provides a way to achieve lower-energy consumption as well as improved performance in thermal energy conversion devices [3–5]. Historically, the observation of the spin Seebeck effect (SSE) in magnetic metals exhibited the interaction between spin and heat currents in a material simultaneously [6]. Moreover, experimental results indicate the existence of SSE in various magnetic phases such as ferromagnetic metals [7], ferromagnetic semiconductors [8], ferromagnetic insulators [9,10], paramagnetic materials [11], antiferromagnetic materials [12], and even nonmagnetic materials by applying a magnetic field [13]. Recently, researchers have been theoretically investigating SSE in two-dimensional materials, in particular planar graphene structures [14,15]. Generally, the existence of ferromagnetic (FM) systems for generating spin-polarized states is a necessary condition for designing graphene-based spin-caloritronics devices. Interestingly, magnetic graphene structures could be more promising than magnetic metals for spin-caloritronics applications [15] due to their long spin relaxation time and length [16].

Graphene exhibits a relatively large Seebeck coefficient theoretically [17] and experimentally [18,19] compared to other materials. However, graphene shows an extremely high thermal conductivity [20], which causes a decrease in the thermoelectric (TE) performance. Cutting graphene into a nanoribbon reduces its thermal conductivity and hence enhances its TE performance. Moreover, graphene nanoribbons (GNRs) have a high Seebeck coefficient due to their direct band gaps [21], and hence, they are a good candidate for TE applications [21–24]. Furthermore, utilizing zigzag-edged GNRs (ZGNRs) with the intrinsic magnetic moments [25,26] is an effective way to produce spin-dependent TE properties. Physically, the localized edge state at the Fermi energy in the presence of the electron-electron interaction suggests the

possibility of magnetic ordering in nanostructures with zigzag edges [27–30]. Spin-dependent TE properties of ZGNRs in the presence of strong magnetic fields and an FM contact with various magnetic alignments [31–38] have been studied. Recently, Sierra *et al.* [39] fabricated a graphene-based spin-caloritronics device and generated a spin voltage using ferromagnetic electrodes. Furthermore, spin and charge TE properties of two overlapping armchair GNRs (AGNRs) using FM electrodes were investigated recently [40]. Interestingly, some work [27–30] based on the intrinsic edge magnetism indicated that spin semiconducting sawtoothlike graphene nanoribbons (ST GNRs) provide an inimitable class of materials that have excellent spin-dependent TE properties, characterized by incomparable values of the giant spin Seebeck coefficient  $S_S$  and the spin figure of merit (FOM). In some rare studies, AGNRs with appropriate designs have been used to produce spin-dependent currents, with [41] or without magnetic fields [42]. However, spin-dependent TE properties based on AGNRs have not been investigated yet.

We designed a spin-caloritronics device based on the intrinsic magnetic moment of a trapezoidal-shaped graphene flake consisting of four zigzag edges bridged between two nonmagnetic (NM) AGNRs. In the proposed scheme, an AGNR is cut in such a way that a nonzero net magnetic moment will be induced in the scattering region of the device, while armchair contacts have a NM ground state. The results indicate a full spin polarization for spin-up and spin-down channels, which are separated by a spin-dependent transmission gap. Moreover, the appearance of spin semiconducting properties with spin-dependent localized transmission peaks around the Fermi level could significantly enhance spin-caloritronics applications based on AGNRs without any magnetic field. Generally, the calculated values of  $S_S$  are comparable to values obtained using ZGNRs as spin-caloritronics devices [29,31,38]. In addition, we created a defect as an antidot in the scattering region to improve the device performance. We found that both  $S_S$  and spin FOM  $Z_S T$  can be modified by changing the antidot position and orientation. Finally, we increased the spin thermoelectric efficiency by controlling the antidot.

\*rfarghadan@kashanu.ac.ir

## II. ATOMIC STRUCTURE AND FORMALISM

### A. Device's atomic structure

The atomic geometry considered in this study was designed based on semi-infinite AGNRs with different widths as left and right contacts, connected by a trapezoidal-shaped graphene flake consisting of four zigzag edges as the scattering region. The designed configuration is shown in Fig. 1(a), where the left and right contacts are 18-AGNRs and 7-AGNRs, respectively. In addition, the scattering region has five atoms per edge, arranged in a zigzag style. Therefore, the atomic configuration shown in Fig. 1(a) is called 18A-5Z-7A. In the presence of the electron-electron interaction, the contacts have an NM ground state because they are a member of the armchair class, whereas the scattering region has an FM ground state. In fact, the special design of the scattering region leads to a nonzero difference between the number of A- and B-sublattice sites [see Fig. 1(a)], and according to the Lieb's theorem [43], it results in the creation of the net magnetic moment of  $m = (N_A - N_B)\mu_B = 5\mu_B$  in the absence of contacts. Therefore, when unpolarized electrons of the left NM contact enter into the scattering region, the edge magnetism of the scattering region creates different spin channels for spin-up and spin-down electrons and hence creates spin-polarized current. In this paper, we consider four atomic structures with different widths for the left contact and the scattering region but with the same width for the right contact [see Fig. 1(b)]. According to the designation of Fig. 1(a), we call the configurations shown in Fig. 1(b) 15A-3Z-7A, 21A-6Z-7A, and 24A-8Z-7A.

### B. Tight-binding and Green's function approach

In order to investigate the electronic properties, we employed the first-nearest-neighbor single  $\pi$ -orbital tight-binding (TB) model and the nonequilibrium Green's function (NEGF) method. The Hamiltonian in the mean-field Hubbard approximation is written as [42]

$$\hat{H}_\sigma = \sum_{i,j,\sigma} (\epsilon_i \delta_{i,j} - t) \hat{d}_{i\sigma}^\dagger \hat{d}_{j\sigma} + U \sum_{i,\sigma} \langle \hat{n}_{i,-\sigma} \rangle \left( \hat{n}_{i,\sigma} - \frac{1}{2} \langle \hat{n}_{i,\sigma} \rangle \right), \quad (1)$$

where  $\hat{d}_{i,\sigma}^\dagger$  and  $\hat{d}_{j,\sigma}$  are fermion creation and annihilation operators at sites  $i$  and  $j$ , respectively,  $\hat{n}_{i,\sigma} = \hat{d}_{i,\sigma}^\dagger \hat{d}_{i,\sigma}$  is the number operator at site  $i$ , and  $\sigma = \uparrow, \downarrow$  denotes the spin index. The hopping integral is  $t = 2.66$  eV for nearest-neighbor interactions.  $U = 1.06t$  is the on-site Coulomb repulsion between electrons of opposite spins [42]. According to the partitioning in Fig. 1, the total Hamiltonian matrix set is divided into submatrices as follows:

$$H_T = H_L + H_R + H_C + H_{CL} + H_{CR}, \quad (2)$$

where  $H_{L,R}$  are the Hamiltonians matrices of the semi-infinite left and right contacts and  $H_{CL}$  and  $H_{CR}$  describe the hopping between the scattering region and the left and right contacts, respectively. Here, we use the TB model for  $H_{CL}$ ,  $H_{CR}$ , and  $H_{L,R}$  because AGNRs have a NM ground state. Furthermore,  $H_C$  is the Hamiltonian matrix of the scattering region, and the mean-field Hubbard approximation is used to calculate  $H_C$ . We neglected the spin-flip scattering [16] and investigated spin-up and spin-down electron transports separately. The Green's function of the scattering region is expressed as [44,45]

$$G_{C,\sigma} = \left[ (\epsilon + i0^+)I - H_{C,\sigma} - \sum_L - \sum_R \right]^{-1}. \quad (3)$$

Here,  $\sum_{L/R} = H_{CL/CR} g_{L/R}(\epsilon) H_{CL/CR}^\dagger$  are called the left/right self-energies, where

$$g_{L/R}(\epsilon) = \left[ (\epsilon + i0^+)I - H_{L/R}^{00} - H_{L/R}^{01} T_{L/R} \right]^{-1} \quad (4)$$

are the surface Green's functions of the contacts.  $H_{L/R}^{00}$  are TB Hamiltonian matrices of the considered unit cell for the left/right contact and  $H_{L/R}^{01}$  are hopping matrices between two adjacent unit cells at the left/right contact.  $T_{L/R}$  are the transfer matrices of the left and right contacts, which can be obtained using an iterative method, as presented in Ref. [45]. The expectation value for the number operator of electrons on each site of the channel is given as [42]

$$\langle \hat{n}_{i,\sigma} \rangle = \left( -\frac{1}{\pi} \right) \int_{-\infty}^{E_F} \text{Im} \langle i, \sigma | G_{C,\sigma}(\epsilon) | i, \sigma \rangle d\epsilon. \quad (5)$$

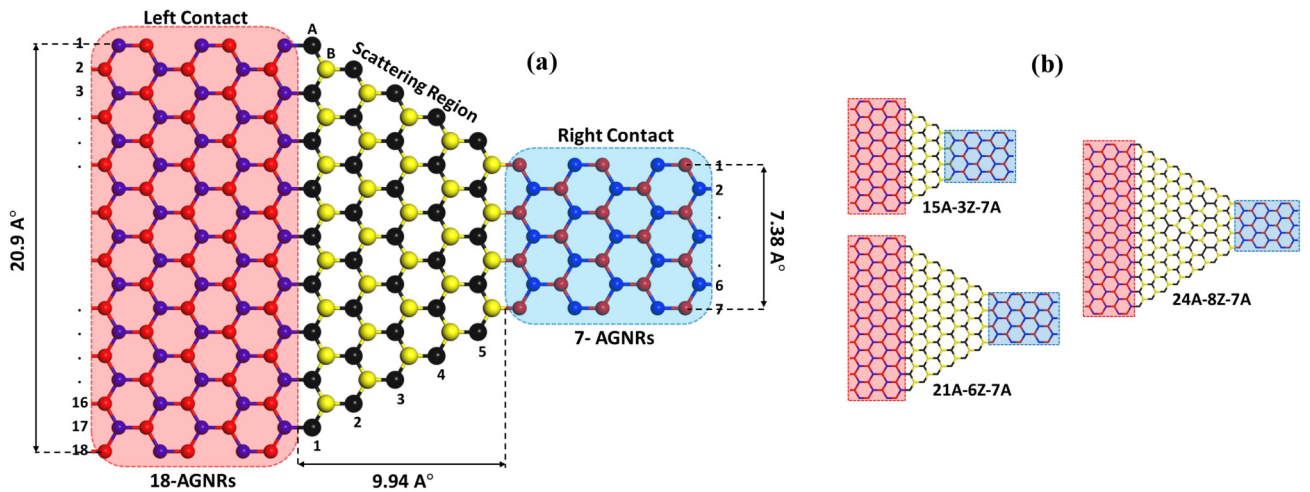


FIG. 1. (a) Schematic structure of a spin-caloritronics device based on AGNR, which is divided into left (18-AGNR) and right (7-AGNR) contacts and the scattering region (a trapezoidal nanoflake). A (black) and B (yellow) atoms illustrate sublattice sites. (b) Other configurations considered in this paper, which are different in terms of the size of their left contact and scattering region, with the same right contact.

Accordingly, the magnetic moment at site  $i$  ( $m_i$ ) of the channel can be expressed as  $m_i = \mu_B[\langle n_{i,\uparrow} \rangle - \langle n_{i,\downarrow} \rangle]$ . In this paper, we solved the mean-field Hubbard Hamiltonian self-consistently using an iterative method [42]. By starting from an antiferromagnetic spin alignment as the initial condition, we construct the Hubbard Hamiltonian [Eq. (1)]. Next, the effect of two semi-infinite AGNRs on the scattering region is added via  $\sum_L$  and  $\sum_R$ , and then the Green's function of the scattering region  $G_{C,\sigma}$ , according to Eq. (3), is calculated. In the last step, the expectation values for the number operators  $\langle n_{i,\sigma} \rangle$  in Eq. (5) at each site and for both spins of electrons are calculated. Finally, the new expectation values of the number operators are substituted in Eq. (1), and this process is iterated until the difference between two successive iterations becomes less than  $10^{-4}$ .

We calculated the electron transmission function from the following equation [44,45]:

$$T_\sigma(\varepsilon) = \text{Tr}[\Gamma_L(\varepsilon)G_{C,\sigma}(\varepsilon)\Gamma_R(\varepsilon)G_{C,\sigma}^\dagger(\varepsilon)], \quad (6)$$

where  $\Gamma_{L/R}(\varepsilon) = -2\text{Im}[\sum_{L/R}(\varepsilon)]$  are the broadening functions that describe the coupling between the left/right contact and the scattering region.

To compute spin-dependent TE coefficients, we must first calculate the electron and phonon transports. The electron-phonon coupling is weak in graphene [46–48], and the electron-phonon mean free path in GNRs is tens of microns at room temperature [49]. Therefore, the electron-phonon interaction was ignored, and thus, the electronic and phononic transports were assumed to be ballistic and independent.

### C. Phonon thermal conductance

To study the phonon's behavior and compute the phonon's contribution to the thermal conductance, we considered the dynamical matrix as [50]

$$D^{(i,j)}(k) = \left( \sum_{j''} K^{(ij'')} - M_i \omega^2(k) I \right) \delta_{i,j} - \sum_{j'} K^{(ij')} e^{ik \cdot \Delta R_{i,j'}}, \quad (7)$$

where  $k, \omega$ , and  $M_i$  are the wave vector, the phonon frequency, and the atomic mass of the  $i$ th carbon atom, respectively, and  $\Delta R_{i,j} = R_i - R_j$  is the relative coordinate of the  $i$ th atom with respect to the  $j$ th atom. Furthermore,  $K^{(ij)}$  represents the  $3 \times 3$  force-constant tensor between the  $i$ th and  $j$ th atoms. In this paper, the dynamical matrix is determined in the four-nearest-neighbor force-constant (4NNFC) model [50]. We used force constants reported by Zimmermann *et al.* [51], which were obtained by fitting on the graphene dispersion curve, calculated by *ab initio* methods. Here, the dynamical matrix  $D$  plays the same role as the Hamiltonian  $H$  for electrons.

In the following, to calculate the phonon transport, we employed the NEGF method, similar to the procedures to calculate the electronic transport. It is enough to replace  $\varepsilon$  with  $M\omega^2$  and  $H$  with  $D$ . Therefore, the phononic Green's function

of the scattering region is given as

$$G_{C,\text{ph}} = \left[ (M\omega^2 + i0^+)I - D_{C,\text{ph}} - \sum_{L,\text{ph}} - \sum_{R,\text{ph}} \right]^{-1}, \quad (8)$$

where  $D_{C,\text{ph}}$  is the dynamical matrix of the scattering region, which is calculated using Eq. (7). Self-energies of phonons  $\sum_{L/R,\text{ph}}$  are expressed based on the dynamical matrix and the surface Green's function, which are obtained using an iterative method similar to the procedures performed for electronic calculations. Eventually, the phonon's contribution to the thermal conductance can be obtained as [27,31]

$$\kappa_{\text{ph}} = \frac{\hbar^2}{2\pi k_B T^2} \int_0^\infty \frac{\omega^2 \exp(\hbar\omega/k_B T)}{[\exp(\hbar\omega/k_B T) - 1]^2} T_{\text{ph}}(\omega) d\omega, \quad (9)$$

where  $T_{\text{ph}}(\omega)$  is the phonon transmission function.

### D. Spin-dependent thermoelectric coefficients

The thermally induced spin-polarized electric current based on the Landauer-Büttiker formalism is given by [52]

$$I_\sigma = \frac{e}{h} \int_{-\infty}^{+\infty} T_\sigma(\varepsilon) [f_L(\varepsilon, T_L) - f_R(\varepsilon, T_R)] d\varepsilon, \quad (10)$$

where  $f_{L(R)}$  is the Fermi-Dirac distribution and  $e, h$ , and  $T$  are the electron charge, Planck constant, and temperature, respectively. According to Eq. (10), the existence of the temperature gradient of  $\Delta T = T_L - T_R$  between two contacts causes a nonzero value of  $f_L - f_R$  and, as a result, the generation of spin-polarized currents with a magnitude that depends on  $\Delta T$  and  $T_{L(R)}$ . The net spin and charge currents are given by  $I_S = I_\uparrow - I_\downarrow$  and  $I_C = I_\uparrow + I_\downarrow$ , respectively. In the following, to calculate the other spin-dependent thermoelectric quantities, we define an intermediate function as [52]

$$L_{n,\sigma}(\mu, T) = -\frac{1}{h} \int (\varepsilon - \mu)^n \frac{\partial f(\varepsilon, \mu, T)}{\partial \varepsilon} T_\sigma(\varepsilon) d\varepsilon, \quad (11)$$

where  $\mu$  is the chemical potential. By assuming a linear-response regime [52],  $\Delta T \rightarrow 0$ , the other spin-dependent thermoelectric quantities such as the Seebeck coefficient, electrical conductance, and the electron's contribution to the thermal conductance are obtained by [31,38]

$$S_\sigma = -\frac{1}{|e|T} \left( \frac{L_{1\sigma}}{L_{0\sigma}} \right), \quad (12)$$

$$G_\sigma = e^2 L_{0\sigma}, \quad (13)$$

$$\kappa_{e,\sigma} = \frac{1}{T} \left( L_{2\sigma} - \frac{L_{1\sigma}^2}{L_{0\sigma}} \right). \quad (14)$$

Finally, by using the coefficients defined above, the spin- and charge-dependent TE efficiency can be characterized by the spin and charge FOM as  $Z_{S(C)}T = S_{S(C)}^2 G_{S(C)} T / (\kappa_e + \kappa_{\text{ph}})$ . Here,  $S_S = (S_\uparrow - S_\downarrow)$  and  $S_C = (S_\uparrow + S_\downarrow)/2$  are the spin and charge Seebeck coefficients, and  $G_S = |G_\uparrow - G_\downarrow|$  and  $G_C = G_\uparrow + G_\downarrow$  are the spin and charge electrical conductance, respectively [15].

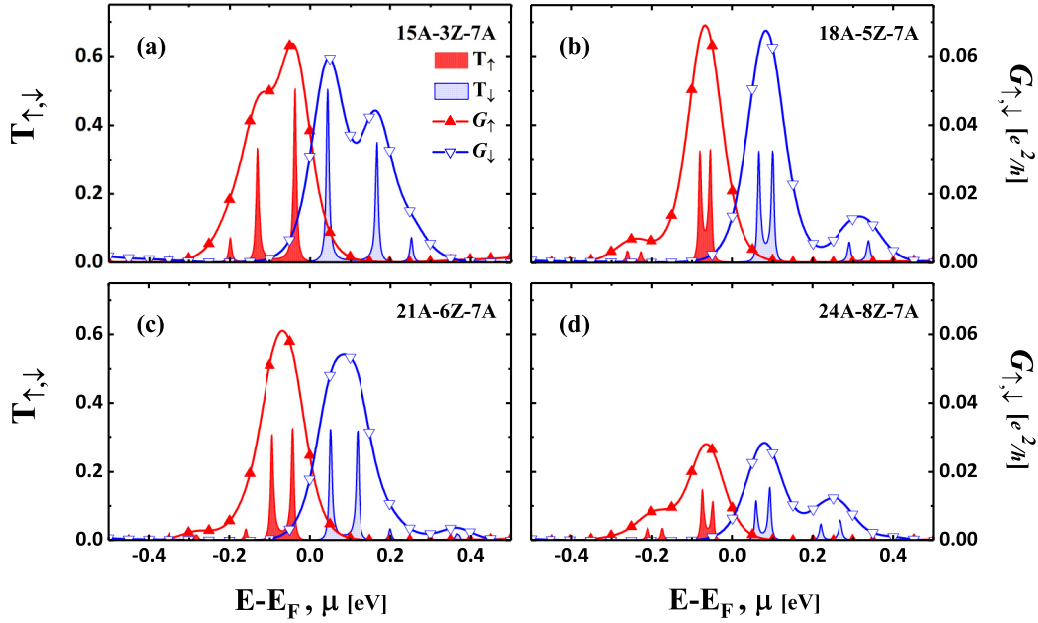


FIG. 2. Transmission coefficients for spin-up (red filled areas) and spin-down (blue filled areas) channels as a function of  $E - E_F$ . The configuration type is specified in each panel. The panels, arranged from (a) to (d), correspond to the smallest through the largest configurations. Colored lines show the spin-dependent conductance as a function of the chemical potential for spin-up (solid symbol) and spin-down (open symbol) channels.

### III. RESULTS AND DISCUSSION

In this paper, we consider four atomic configurations with the same geometry but with different sizes, as presented in Fig. 1. The main difference between the considered configurations is in the size of their left contacts and scattering regions, while the size of the right contacts is equal in all of the configurations. The variation in the width of the left contacts and the variation in the size of the scattering regions are interdependent; as the width of the left contact increases, the size of the scattering region increases. The unique feature of this geometry is the utilization of AGNRs as the left and right contacts with a trapezoidal-shaped graphene flake consisting of four zigzag edges, whereas an FM ZGNR was used in other geometries for studying spin-caloritronics effects. However, AGNRs lead to the observation of SSE and also good spin-caloritronics effects in this system. This can be attributed to the existence of a nonzero magnetic moment in only a small part of the device as the scattering region with AGNR contacts. It is completely clear that the net magnetic moment of the designed systems in Fig. 1 increases as the length of the zigzag edges increases. This is quite evident when one considers the values of  $1.65\mu_B$ ,  $2.72\mu_B$ ,  $3.58\mu_B$ , and  $4.64\mu_B$  for 15A-3Z-7A, 18A-5Z-7A, 21A-6Z-7A, and 24A-8Z-7A, respectively. Note that the spin correlation length for magnetic graphene edges is about 1 nm at room temperature [53]. Therefore, considering the size of the zigzag edges in the considered configurations, the spin correlation is preserved in the scattering region, in contrast to ZGNRs, where the spin correlation length should be preserved over the length of semi-infinite contacts.

Spin-polarized transmission coefficients  $T_{\uparrow,\downarrow}$  in the region around the Fermi level are plotted in Fig. 2 for the four configurations in separate panels, as indicated by the filled areas. The panels are arranged from Figs. 2(a) to 2(d), corre-

sponding to the smallest through largest configurations, and the Fermi level was set to zero. The most important aspect of the designed AGNR is its spin semiconducting properties with tunable spin-dependent transmission gaps, which are useful for spin-caloritronics applications. As can be seen, the localized transmission peaks around the Fermi level show that only spin-up electrons can pass below the Fermi level, while spin-down electrons can pass only above the Fermi level. Furthermore, spin-up and spin-down transmissions are separated by the transport gap from each other. Moreover, the transport gaps are about 0.08, 0.12, 0.093, and 0.1 eV for the 15A-3Z-7A, 18A-5Z-7A, 21A-6Z-7A, and 24A-8Z-7A configurations, respectively [see Figs. 2(a)–2(d)], and hence, the variation in the system size changes the transport gap. Furthermore, the existence of the spin-dependent transmission gap and the localized transmission peaks around the Fermi level in all of the configurations could produce a full spin polarization and a large Seebeck coefficient near the values reported for ST GNRs [27]. The computed values indicate that the transmission coefficient depends highly on the system size; however, spin-up and spin-down channels are symmetrical around the Fermi level in all of the configurations. This electron-hole symmetry with the spin-dependent transmission gap could produce high-symmetry thermal spin-up and spin-down currents.

To clarify, the spin-dependent electrical conductance  $G_{\uparrow,\downarrow}$  as a function of the chemical potential is also presented in each panel in Fig. 2. In some ranges of the chemical potential, the conductance is zero in one spin channel, while another channel is conductive. Therefore, in some ranges of the chemical potential, our proposed device produces a fully spin polarized current. However, approximately inside the region of the transport gap, both  $G_{\uparrow}$  and  $G_{\downarrow}$  are conductive, so that the spin polarization decreases in this region. Interestingly,



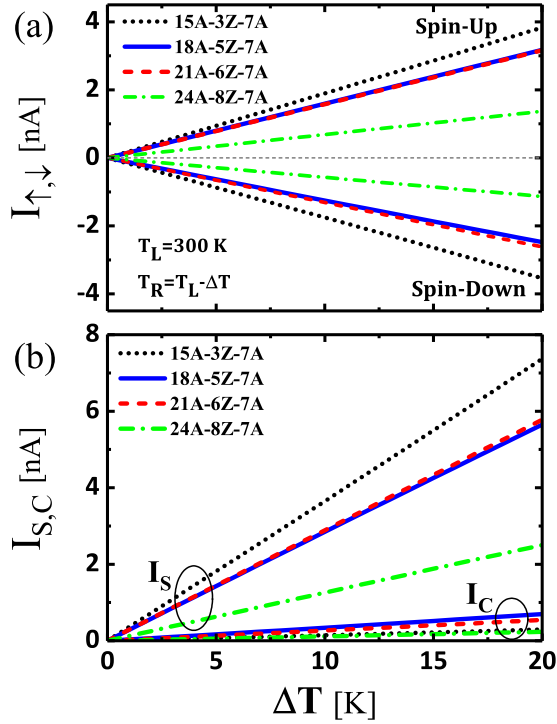


FIG. 3. (a) Thermally induced spin-polarized currents ( $I_{\uparrow}$ ,  $I_{\downarrow}$ ) and (b) spin and charge currents ( $I_S$  and  $I_C$ ) as a function of  $\Delta T$  at  $T_L = 300$  K for different configurations.

$G_{\uparrow}$  and  $G_{\downarrow}$  are equal in magnitude at  $\mu \simeq 0$  eV, which leads to a zero spin-dependent conductance and a nonzero charge-dependent conductance for all of the configurations. Generally, it can be concluded that configurations of different sizes have a similar spin semiconducting behavior in creating spin polarization properties. However, the quantitative behavior of spin-dependent properties, such as the transport gap and the maximum transmission, could be adjusted by changing the system size.

For more clarification, it should be said that according to Eq. (10) and spin-polarized transmission coefficients (Fig. 2), when a temperature gradient  $\Delta T$  is applied across the two contacts,  $f_L - f_R$  is no longer equal to zero, and as a result, a thermal spin current is induced. Figure 3(a) shows thermally

spin polarized currents  $I_{\sigma}$  as a function of  $\Delta T$  for  $T_L = 300$  K in  $\mu = 0$  for the different configurations. Clearly,  $I_{\uparrow}$  and  $I_{\downarrow}$  flow in opposite directions, demonstrating the existence of SSE in designed AGNRs. High symmetry between  $I_{\uparrow}$  and  $I_{\downarrow}$  relative to  $Y = 0$  axis leads to almost zero charge current and hence could produce a net spin current. As can be seen in Fig. 3(b),  $I_C$  always has a value less than 1 nA in the region  $\Delta T = 0-20$  K, while a significant increase in  $I_S$  is observed with increasing  $\Delta T$ , in particular for the 15A-3Z-7A, 18A-5Z-7A, and 21A-6Z-7A configurations.

The electron contribution to the thermal conductance  $\kappa_e$  as a function of the chemical potential is presented in Fig. 4(a). The values of  $\kappa_e$  were calculated at  $T = 300$  K for the considered configurations. As can be seen, the curve behavior of  $\kappa_e$  is almost the same for different configurations. However, from a quantitative perspective, they have dissimilar maximum values. The maximum value of  $\kappa_e$  is about  $15 \times 10^{-3}$  nW/K for the 15A-3Z-7A configuration, while the values of  $\kappa_e$  are lower for the other configurations. The maximum values for the 18A-5Z-7A, 21A-6Z-7A, and 24A-8Z-7A configurations are about  $5.6 \times 10^{-3}$ ,  $7.3 \times 10^{-3}$ , and  $5.3 \times 10^{-3}$  nW/K, which are 62.66%, 51.33%, and 64.66%, respectively, lower than that of the 15A-3Z-7A configuration. This can be attributed to the different number of carbon chains in the right and left contacts, so that as this difference increases, the value of  $\kappa_e$  decreases. Of course, it does not decrease uniformly. By comparing Figs. 2 and 4(a), it is obvious that the behavior of  $\kappa_e$  is similar to that of  $T_{\uparrow, \downarrow}$  or  $G_{\uparrow, \downarrow}$ . In this regard, the peaks of  $\kappa_e$  below and above the Fermi level correspond to spin-up and spin-down states, respectively.

In addition, the phonon contribution to the thermal conductance  $\kappa_{ph}$  was calculated as a function of temperature for the four configurations, and the results are presented in Fig. 4(b). As can be seen, there is a little difference in  $\kappa_{ph}$  values between the configurations, especially at low temperatures. However, as the temperature increases, the difference increases too. For example, the minimum value of  $\kappa_{ph}$  at  $T = 300$  K (0.81 nW/K) for the 15A-3Z-7A configuration rises to the maximum value of 0.86 nW/K for the 24A-8Z-7A one. However, these values are approximately 3 times lower than  $\kappa_{ph}$  of the 16-AGNR configuration, which is 2.3 nW/K at room temperature [24]. This is due to the atomic geometry shown in Fig. 1, especially the edge roughness of the scattering region and difference between the width of left and right contacts, which consequently

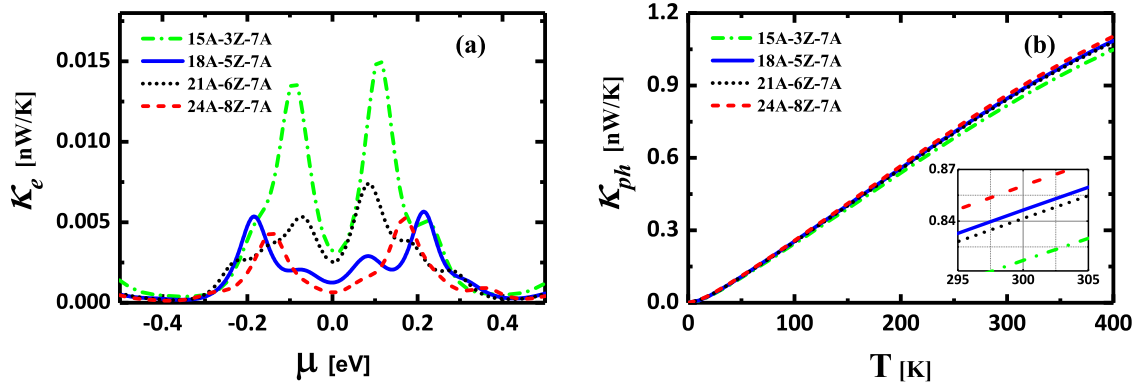


FIG. 4. (a) The electron thermal conductance as a function of the chemical potential at  $T = 300$  K and (b) the phonon thermal conductance as a function of temperature for the structures shown in Fig. 1.

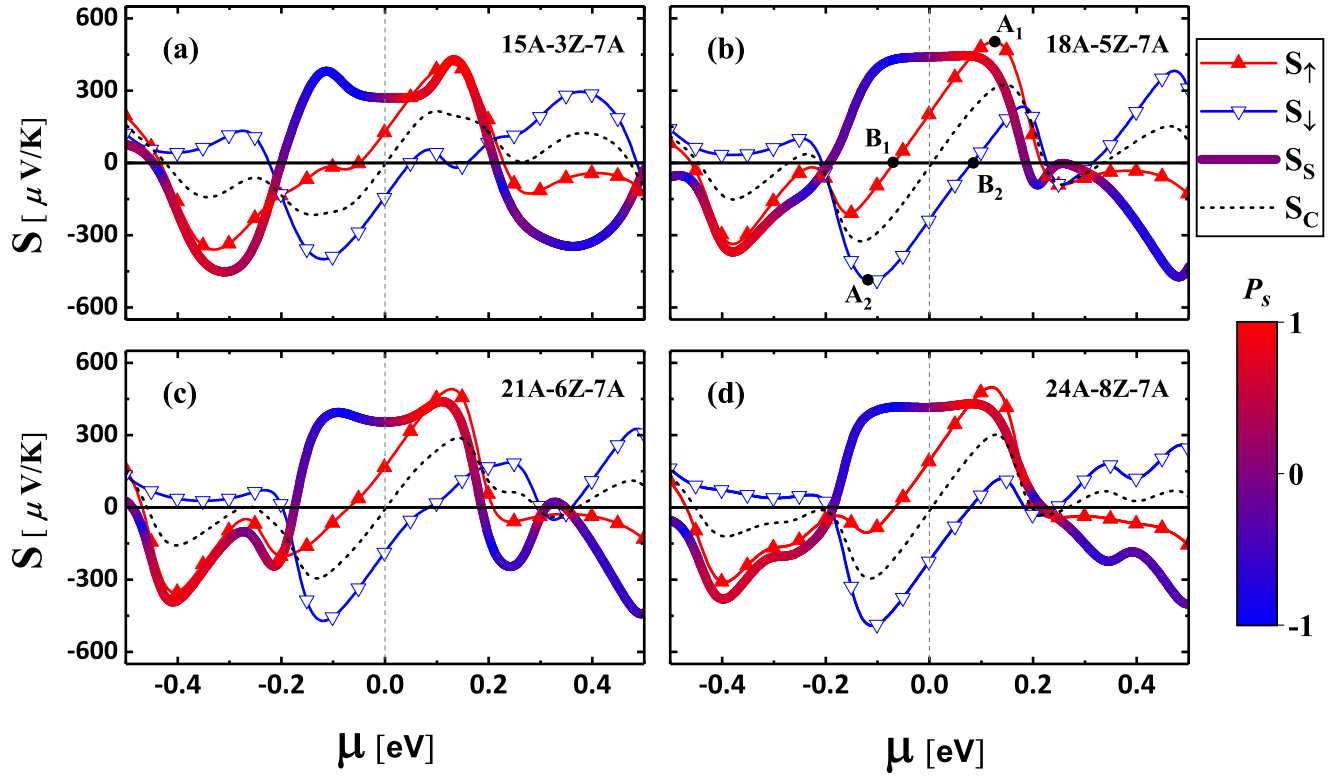


FIG. 5. Spin (colored solid line) and charge (black dashed line) Seebeck coefficients and spin-up (solid symbol) and spin-down (open symbol) Seebeck coefficients as a function of the chemical potential at room temperature. The color of  $S_S$  changes according to Seebeck polarization.

suppresses some phonon modes and reduces  $\kappa_{ph}$  compared to that of a pristine AGNR. A comparison of the values of  $\kappa_{ph}$  and  $\kappa_e$  indicates that the electron thermal conductance is about 1% of the phonon thermal conductance, which is similar to the behavior reported for a graphene sheet [54]. Therefore, phonons are responsible for the heat transfer in these structures.

Now, we investigate Seebeck coefficients for all of the configurations, which are depicted in Fig. 1. Values of spin-up ( $S_\uparrow$ ) and spin-down ( $S_\downarrow$ ) Seebeck coefficients as well as spin-dependent ( $S_S$ ) and charge-dependent ( $S_C$ ) Seebeck coefficients as a function of the chemical potential are shown in Fig. 5. At first glance, a large SSE can be found in designed AGNRs, which is due to their spin semiconducting behavior and localized spin-dependent transmission spectra. Generally, a similar behavior can be seen for  $S_\uparrow$  and  $S_\downarrow$  in all four configurations, in particular in the range of  $\mu \simeq (-0.2, 0.2)$  eV. The maximum absolute values of  $S_\uparrow$  and  $S_\downarrow$ , denoted as points A1 and A2 in Fig. 5(b), correspond to the 18A-5Z-7A configuration. The values are 503 and 493  $\mu\text{V/K}$ , which are located at  $\mu = 0.12$  eV and  $\mu = -0.11$  eV for  $S_\uparrow$  and  $S_\downarrow$ , respectively. The values are comparable to the values reported for devices based on ZGNRs. For example, maximum absolute values of  $S_\uparrow$  and  $S_\downarrow$  are about 20 and 600  $\mu\text{V/K}$ , respectively, for all-carbon nanojunctions at room temperature [29]. As can be seen, for several values of the chemical potential, for example, points B1 and B2 in Fig. 5(b), either  $S_\uparrow$  or  $S_\downarrow$  is zero, while the other one is nonzero. This can be attributed to the neutralization of electron and hole currents by each other in one of the spin channels and the existence of a thermally induced

spin-polarized current in another one, as expected from the thermoelectric behavior of spin semiconductors.

Furthermore, as shown in Fig. 5, at  $\mu = 0.005$  eV (dashed line in each panel),  $S_\uparrow$  and  $S_\downarrow$  have the same value with opposite signs, and hence,  $S_C$  (black dashed line) is zero, while  $S_S$  (colored solid line) is nonzero, for all configurations. This indicates that at  $\mu = 0.005$  eV, a temperature gradient induces a pure spin current without any charge current, generating a zero-charge voltage and a nonzero spin voltage ( $V_S = S_S \Delta T$ ) based on AGNRs. Physically, at this point, the transport is mediated by both spin-up holes and spin-down electrons with an equal magnitude but opposite directions of current, and hence, a thermal gradient could induce a pure spin current in  $\mu \simeq 0$  eV.

As shown in Fig. 5, the variation of  $S_S$  inside the transport gap and sometimes across the localized transmission peaks [Figs. 5(b) and 5(d)] is very small, and it is seen that  $S_S$  is approximately flat. The rather flat region is also observed for ST GNR [27] due to the constant difference between  $S_\uparrow$  and  $S_\downarrow$ , which is related to the inversely symmetric Seebeck coefficients between the spin channels and their linear dependence on the chemical potential, and could enhance TE efficiency [27]. The value of  $S_S$  in this region is strongly dependent on the transport gap, so that as the transport gap increases from 0.08 eV [see Fig. 5(a)] to 0.12 eV [see Fig. 5(b)], the value of  $S_S$  increases too by 60%. For the 18A-5Z-7A configuration, the maximum value of  $S_S$  in the transport gap region is 445  $\mu\text{V/K}$ , and it reaches 473  $\mu\text{V/K}$  outside of this region. These values are approximately 10 times higher than the value reported for

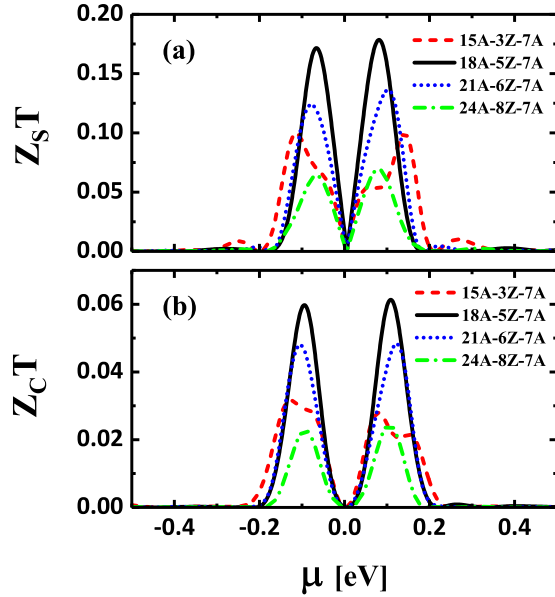


FIG. 6. (a) Spin and (b) charge FOMs as a function of the chemical potential at  $T = 300$  K.

graphene-based molecular junctions, which have a maximum value of  $45 \mu\text{V/K}$  at  $T = 150$  K [38]. Interestingly, the high values of  $S_S$  and  $G_S$  inside the transmission gap improve the spin TE efficiency. In order to show the effect of each spin channel on  $S_S$  separately, the Seebeck polarization is also illustrated. The color of  $S_S$  in Fig. 5 changes according to the Seebeck polarization,  $P_S = (|S_\uparrow| - |S_\downarrow|) / (|S_\uparrow| + |S_\downarrow|)$ . As can be seen, for all of the configurations, the color of  $S_S$  tends to blue in the region of  $\mu \simeq (-0.2, 0)$ , while it tends to red in the region of  $\mu \simeq (0, 0.2)$ , because  $S_\downarrow$  is dominant in the first region and  $S_\uparrow$  is dominant in the second region. The positive (negative) sign of  $S_\uparrow$  or  $S_\downarrow$  is related to the  $p$ -type ( $n$ -type) nature of the device. Clearly, when  $S_\uparrow$  is dominant,  $S_S$  and  $S_C$  have the same sign, but when  $S_\downarrow$  is dominant, their signs are opposite.

Finally, to investigate spin and charge TE efficiencies, we calculated  $Z_S T$  and  $Z_C T$  for the considered systems. The results are shown in Fig. 6, where  $Z_S T$  and  $Z_C T$  are plotted as a function of the chemical potential. The results indicate that changing the system size has a significant effect on the enhancement of the TE efficiency. It is clearly seen that the 18A-5Z-7A configuration has the highest spin and charge TE efficiencies. Since  $\kappa_{ph}$  is almost equal for all of the configurations [see Fig. 4(b)] and  $\kappa_e$  is insignificant compared to the phonon thermal conductance [see Fig. 4(a)], the difference in the values of TE efficiencies between these systems is related to the Seebeck and electrical conductance values. Furthermore, maximum values of  $Z_S T$  and  $Z_C T$  lie in the transport gap region.

#### IV. THE EFFECT OF AN ANTIDOT ON SPIN CALORITRONICS

In this section, we investigate the effect of an antidot on spin-dependent TE properties for the proposed structure. For this purpose, we considered a defect in the form of a triangular

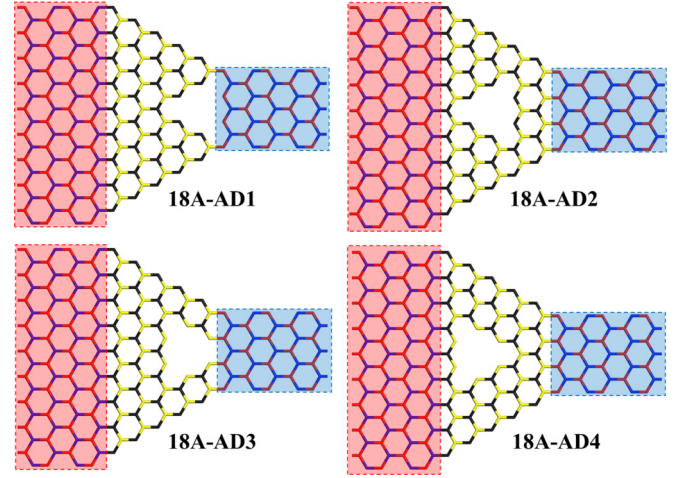


FIG. 7. Schematic view of configurations with antidots with different positions and orientations in the channel. The antidots are created in the 18A-5Z-7A configuration.

antidot in the scattering region (channel) for the 18A-5Z-7A configuration. Then, we examined the effect of the antidot position and orientation relative to the channel on spin-dependent TE properties. The atomic configurations with antidots are shown in Fig. 7 and are named 18A-AD1, 18A-AD2, 18A-AD3, and 18A-AD4. The antidot orientation in the 18A-AD1 and 18A-AD2 configurations is opposite to that in the 18A-AD3 and 18A-AD4 configurations. Furthermore, the antidots in the 18A-AD1 and 18A-AD3 configurations are located at the interface of the channel and the right contact. However, the antidots in the 18A-AD2 and 18A-AD4 configurations are located at the center of the channel. The presence of an antidot in the 18A-AD1 and 18A-AD2 configurations increases the difference between the number of A- and B-sublattice atoms, and hence, the net magnetic moment increases compared to the perfect state [see Fig. 1(a)]. However, the situations of the other two configurations are exactly opposite those of the 18A-AD1 and 18A-AD2 configurations. The net magnetic moment in the 18A-AD1 and 18A-AD2 configurations is  $3.5\mu_B$ , and it is  $1.5\mu_B$  in the 18A-AD3 and 18A-AD4 configurations.

The phonon thermal conductance for the antidot-included configurations is presented in Fig. 8, and the values of  $\kappa_{ph}$  for the nondefect configuration are also shown.  $\kappa_{ph}$  is lower

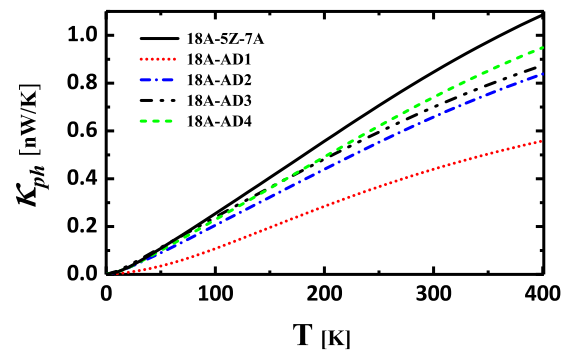


FIG. 8. The phonon thermal conductance as a function of temperature for antidot-included configurations.

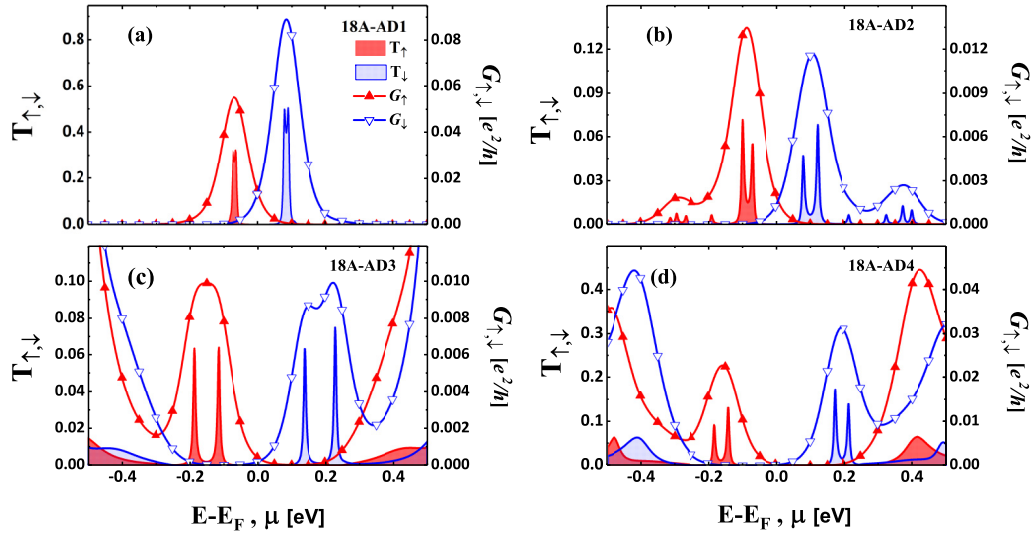


FIG. 9. Transmission coefficients for spin-up (red filled areas) and spin-down (blue filled areas) channels as a function of  $E - E_F$ . Spin-up (solid symbols) and spin-down (open symbols) electrical conductance values as a function of the chemical potential for the antidot-included configuration at  $T = 300$  K.

than that of the nondefect configuration, but the percentages of the decreases are different for different configurations, and the 18A-AD1 configuration has the highest decrease.  $\kappa_{ph}$  at  $T = 300$  K for the 18A-AD1 configuration is approximately 47% lower than that of the 18A-5Z-7A configuration. This can be attributed to the antidot location and orientation in the 18A-AD1 configuration, which leads to a reduction in the number of connective atoms between the channel and the right contact. In view of that fact, the phonon transport is strongly suppressed in the 18A-AD1 configuration compared to the other configurations. A decrease in  $\kappa_{ph}$  increases the TE efficiency, and hence, the 18A-AD1 configuration has a better effect.

Spin-polarized transmission coefficients as a function of  $E - E_F$  and spin-dependent electrical conductance as a function of the chemical potential are presented in Fig. 9. As can be seen, the spin semiconducting property is preserved in these structures, even in the presence of an antidot in their channels. Furthermore, the presence of an antidot in the channel could enhance the transport gap and preserve the localized transmission peaks around the Fermi level, despite the fact that the net magnetization decreases in the channel for 18A-AD3 and 18A-AD4 [see Figs. 9(c) and 9(d)]. The transport gaps are about 0.142, 0.152, 0.253, and 0.313 eV for the 18A-AD1, 18A-AD2, 18A-AD3, and 18A-AD4 configurations, respectively. The comparison of Figs. 9(a) and 9(b) with Figs. 9(c) and 9(d) demonstrates that changing the antidot orientation in the 18A-AD3 and 18A-AD4 configurations relative to the 18A-AD1 and 18A-AD2 configurations significantly increases the transport gap. Moreover, changing the antidot position and orientation changes the values of transmission and electrical conductance. Interestingly, maximum values of  $T_{\downarrow}$  and  $G_{\downarrow}$  [see Fig. 9(a)] are approximately 55% and 30% higher than those of the 18A-5Z-7A configuration, while maximum values of  $T_{\uparrow}$  and  $G_{\uparrow}$  are slightly lower. As a result, modifications of the spin-dependent electron transport depend on the antidot position and orientation, and the spin semiconducting properties and

the intensity of the induced spin-dependent currents can be controlled by engineering the antidot.

The spin-dependent Seebeck coefficient as a function of the chemical potential is shown in Fig. 10(a) at  $T = 300$  K for the proposed configurations. As can be seen, the variation of the antidot position and orientation modifies the values of  $S_S$ , and the modifications are particularly evident inside the transport gap region. It is observed that as the transport gap increases from 0.142 eV in Fig. 9(a) to 0.313 eV in Fig. 9(d),  $S_S$  gradually increases, which is evident in Fig. 10(a). This is consistent with the results mentioned in Sec. III, where  $S_S$

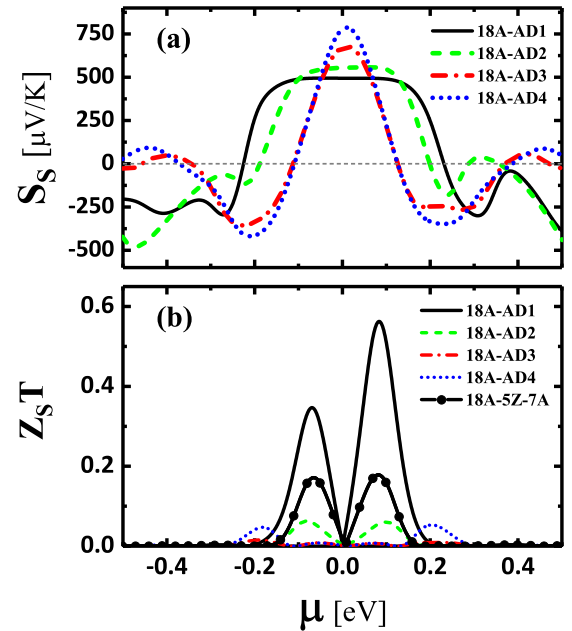


FIG. 10. (a) The spin Seebeck coefficient and (b) spin FOM as a function of the chemical potential at  $T = 300$  K for the configurations presented in Fig. 7.



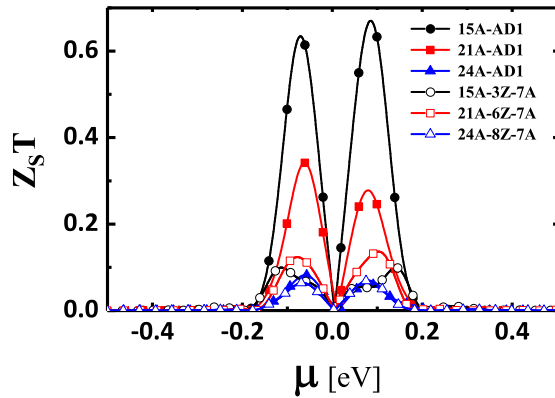


FIG. 11. The spin FOM for the 15A-3Z-7A, 21A-6Z-7A, and 24A-8Z-7A configurations with antidots of the AD1 type. The results regarding configurations without antidots are also provided for comparison (the results are calculated at  $T = 300$  K).

increases as the spin-dependent transmission gap increases. Furthermore, by comparing  $S_S$  values corresponding to the 18A-AD1 and 18A-AD2 configurations and those corresponding to the 18A-AD3 and 18A-AD4 configurations [Fig. 10(a)], we conclude that changing the antidot orientation leads to more variation in  $S_S$ , especially in the transport gap region. In the 18A-AD4 configuration, the maximum value of  $S_S$  in this region is  $786 \mu\text{V/K}$ , which is 76% higher than that of the configuration without an antidot. The 18A-AD1 and 18A-AD4 configurations have the lowest and highest transport gaps, respectively [see Figs. 9(a) and 9(d)].

Finally, the spin-dependent TE efficiency was determined using the spin FOM relation and also the coefficients calculated from electron and phonon transports. The results are presented in Fig. 10(b) as a function of the chemical potential for antidot-included configurations, and  $Z_S T$  of the pristine configuration is also shown for comparison. The maximum value of  $Z_S T$  for the 18A-AD1 configuration is higher than that for the pristine configuration; however, it is lower for the other configurations. This demonstrates that controlling the antidot can play a significant role in the improvement of the TE efficiency.

As shown in Fig. 10(b), the percentage increase in  $Z_S T$  for 18A-AD1 compared with that for 18A-5Z-7A is different for spin-up and spin-down states, so the maximum values of  $Z_S T$  below and above the Fermi level are 2 and 3.1 times larger, respectively. By considering the spin FOM relation [ $Z_S T = S_S^2 G_S T / (\kappa_e + \kappa_{ph})$ ] and neglecting the contribution of electrons ( $\kappa_e = 0.01\kappa_{ph}$ ), we found that because of the rather flat plateau in  $S_S$  around the Fermi level, the asymmetry of  $Z_S T$  originates from the asymmetry of  $G_\uparrow$  and  $G_\downarrow$  in the 18A-AD1 configuration [see Fig. 9(a)]. Moreover, for the 18A-AD2, 18A-AD3, and 18A-AD4 configurations, the maximum value of  $S_S$  occurs in the energy region where  $G_S$  is lower. Thus,  $Z_S T$

decreases sensitively in the presence of an antidot. However, in the 18A-AD1 configuration, the position of the maximum values of  $S_S$  and  $G_S$  occurs in the same energy region, and due to the point contact,  $\kappa_{ph}$  decreases more than in the other cases. Therefore,  $Z_S T$  increases more in this case than in the other configurations [see Fig. 10(b)].

For further clarification, we considered the other configurations presented in Fig. 1 with an antidot with the same position as in 18A-AD1, and then we investigated spin-dependent TE coefficients. The results for  $Z_S T$  are shown in Fig. 11. As can be seen, in the smaller configuration (15A-AD1), the antidot has a greater impact on the increase in efficiency, so that  $Z_S T$  in this configuration is about 7 times higher than that in the configuration without an antidot. As the system size increases, the effectiveness of antidots in improving the efficiency gradually decreases, which is due to the increase in the phonon thermal conductance (see Fig. 8). Generally, antidots have various effects on the spin-dependent Seebeck coefficient and the spin FOM. However, by engineering the position, orientation, and geometry of the antidot,  $S_S$  and  $Z_S T$  can be separately enhanced.

## V. CONCLUSIONS

In summary, using the mean-field Hubbard model and the Landauer-Büttiker transport formalism, we investigated the possibility of improving the spin TE performance of AGNR-based devices. The results demonstrated that the designed device behaves like a spin semiconductor, which is due to the existence of a spin-dependent transmission gap. The unique feature of this design is the existence of narrow peaks in its transmission, which plays a significant role in the creation of a relatively large  $S_S$  compared to that in other materials. It was observed that an increase in the transport gap leads to an increase in  $S_S$ . Furthermore, in order to improve the efficiency, we considered an antidot in different positions and directions of the scattering region. The results proved that the variation of the antidot situation strongly affects the spin-dependent TE properties, so that by engineering the antidot defects, we can increase the spin transmission gap, which leads to an increase in  $S_S$  to about  $800 \mu\text{V/K}$ . Finally, we demonstrated that the presence of an antidot, if it were located in an appropriate situation, would improve the system performance, and the improvement depends on the system size. The results showed that engineering defects can be effective for the enhancement of the spin TE efficiency in AGNRs.

## ACKNOWLEDGMENT

This work financially supported by the Iran National Support Foundation (INSF).

- [1] S. Wolf, D. Awschalom, R. Buhrman, J. Daughton, S. Von Molnar, M. Roukes, A. Y. Chtchelkanova, and D. Treger, *Science* **294**, 1488 (2001).
- [2] I. Žutić, J. Fabian, and S. Das Sarma, *Rev. Mod. Phys.* **76**, 323 (2004).

- [3] M. Johnson, *Solid State Commun.* **150**, 543 (2010).
- [4] G. E. Bauer, E. Saitoh, and B. J. Van Wees, *Nat. Mater.* **11**, 391 (2012).
- [5] S. R. Boona, R. C. Myers, and J. P. Heremans, *Energy Environ. Sci.* **7**, 885 (2014).

- [6] K. Uchida, S. Takahashi, K. Harii, J. Ieda, W. Koshibae, K. Ando, S. Maekawa, and E. Saitoh, *Nature (London)* **455**, 778 (2008).
- [7] S. Bosu, Y. Sakuraba, K.-i. Uchida, K. Saito, T. Ota, E. Saitoh, and K. Takanashi, *Phys. Rev. B* **83**, 224401 (2011).
- [8] C. Jaworski, J. Yang, S. Mack, D. Awschalom, J. Heremans, and R. Myers, *Nat. Mater.* **9**, 898 (2010).
- [9] K.-i. Uchida, H. Adachi, T. Ota, H. Nakayama, S. Maekawa, and E. Saitoh, *Appl. Phys. Lett.* **97**, 172505 (2010).
- [10] K. Uchida, J. Xiao, H. Adachi, J.-i. Ohe, S. Takahashi, J. Ieda, T. Ota, Y. Kajiwara, H. Umezawa, H. Kawai *et al.*, *Nat. Mater.* **9**, 894 (2010).
- [11] S. M. Wu, J. E. Pearson, and A. Bhattacharya, *Phys. Rev. Lett.* **114**, 186602 (2015).
- [12] S. M. Wu, W. Zhang, A. KC, P. Borisov, J. E. Pearson, J. S. Jiang, D. Lederman, A. Hoffmann, and A. Bhattacharya, *Phys. Rev. Lett.* **116**, 097204 (2016).
- [13] C. Jaworski, R. Myers, E. Johnston-Halperin, and J. Heremans, *Nature (London)* **487**, 210 (2012).
- [14] M. Inglot, V. K. Dugaev, and J. Barnaś, *Phys. Rev. B* **92**, 085418 (2015).
- [15] B. Z. Rameshti and A. G. Moghaddam, *Phys. Rev. B* **91**, 155407 (2015).
- [16] N. Tombros, S. Tanabe, A. Veligura, C. Jozsa, M. Popinciuc, H. T. Jonkman, and B. J. van Wees, *Phys. Rev. Lett.* **101**, 046601 (2008).
- [17] D. Dragoman and M. Dragoman, *Appl. Phys. Lett.* **91**, 203116 (2007).
- [18] Y. M. Zuev, W. Chang, and P. Kim, *Phys. Rev. Lett.* **102**, 096807 (2009).
- [19] P. Wei, W. Bao, Y. Pu, C. N. Lau, and J. Shi, *Phys. Rev. Lett.* **102**, 166808 (2009).
- [20] A. A. Balandin, S. Ghosh, W. Bao, I. Calizo, D. Teweldebrhan, F. Miao, and C. N. Lau, *Nano Lett.* **8**, 902 (2008).
- [21] H. Zheng, H. Liu, X. Tan, H. Lv, L. Pan, J. Shi, and X. Tang, *Appl. Phys. Lett.* **100**, 093104 (2012).
- [22] Y. Ouyang and J. Guo, *Appl. Phys. Lett.* **94**, 263107 (2009).
- [23] H. Sevinçli and G. Cuniberti, *Phys. Rev. B* **81**, 113401 (2010).
- [24] F. Mazzamuto, V. H. Nguyen, Y. Apertet, C. Caër, C. Chassat, J. Saint-Martin, and P. Dollfus, *Phys. Rev. B* **83**, 235426 (2011).
- [25] O. V. Yazyev, *Rep. Prog. Phys.* **73**, 056501 (2010).
- [26] G. Z. Magda, X. Jin, I. Hagymási, P. Vancsó, Z. Osváth, P. Nemes-Incze, C. Hwang, L. P. Biro, and L. Tapasztó, *Nature (London)* **514**, 608 (2014).
- [27] X. Chen, Y. Liu, B.-L. Gu, W. Duan, and F. Liu, *Phys. Rev. B* **90**, 121403 (2014).
- [28] Q.-B. Liu, D.-D. Wu, and H.-H. Fu, *Phys. Chem. Chem. Phys.* **19**, 27132 (2017).
- [29] X. Yang, H. Wang, Y. Chen, Y. Kuang, X. Hong, Y. Liu, J. Feng, and X. Wang, *Phys. Chem. Chem. Phys.* **17**, 22815 (2015).
- [30] Y. Liu, X. Shao, T. Shao, J. Zhang, Y. Kuang, D. Zhang, Z. Shao, H. Yu, X. Hong, J. Feng *et al.*, *Carbon* **109**, 411 (2016).
- [31] M. Wierzbicki, R. Swirkowicz, and J. Barnaś, *Phys. Rev. B* **88**, 235434 (2013).
- [32] M. Zeng, Y. Feng, and G. Liang, *Nano Lett.* **11**, 1369 (2011).
- [33] S.-g. Cheng, *J. Phys.: Condens. Matter* **24**, 385302 (2012).
- [34] Y. Ni, K. Yao, H. Fu, G. Gao, S. Zhu, and S. Wang, *Sci. Rep.* **3**, 1380 (2013).
- [35] M. Zeng, Y. Feng, and G. Liang, *Appl. Phys. Lett.* **99**, 123114 (2011).
- [36] Y.-S. Liu, X.-F. Wang, and F. Chi, *J. Mater. Chem. C* **1**, 8046 (2013).
- [37] M. Zeng, W. Huang, and G. Liang, *Nanoscale* **5**, 200 (2013).
- [38] J. Li, B. Wang, F. Xu, Y. Wei, and J. Wang, *Phys. Rev. B* **93**, 195426 (2016).
- [39] J. F. Sierra, I. Neumann, J. Cuppens, B. Raes, M. V. Costache, and S. O. Valenzuela, *Nat. Nanotechnol.* **13**, 107 (2018).
- [40] L. Chico, P. A. Orellana, L. Rosales, and M. Pacheco, *Phys. Rev. Appl.* **8**, 054029 (2017).
- [41] Z.-Y. Zhang and W. Guo, *Carbon* **115**, 43 (2017).
- [42] A. Saffarzadeh and R. Farghadan, *Appl. Phys. Lett.* **98**, 023106 (2011).
- [43] E. H. Lieb, *Phys. Rev. Lett.* **62**, 1201 (1989).
- [44] F. Muñoz-Rojas, D. Jacob, J. Fernández-Rossier, and J. J. Palacios, *Phys. Rev. B* **74**, 195417 (2006).
- [45] M. Buongiorno Nardelli, *Phys. Rev. B* **60**, 7828 (1999).
- [46] R. Bistritzer and A. H. MacDonald, *Phys. Rev. Lett.* **102**, 206410 (2009).
- [47] J. C. W. Song, M. Y. Reizer, and L. S. Levitov, *Phys. Rev. Lett.* **109**, 106602 (2012).
- [48] J. F. Sierra, I. Neumann, M. V. Costache, and S. O. Valenzuela, *Nano Lett.* **15**, 4000 (2015).
- [49] D. Gunlycke, H. M. Lawler, and C. T. White, *Phys. Rev. B* **75**, 085418 (2007).
- [50] R. Saito, G. Dresselhaus, and M. S. Dresselhaus, *Physical Properties of Carbon Nanotubes* (World Scientific, Singapore, 1998).
- [51] J. Zimmermann, P. Pavone, and G. Cuniberti, *Phys. Rev. B* **78**, 045410 (2008).
- [52] U. Sivan and Y. Imry, *Phys. Rev. B* **33**, 551 (1986).
- [53] O. V. Yazyev and M. I. Katsnelson, *Phys. Rev. Lett.* **100**, 047209 (2008).
- [54] A. A. Balandin, *Nat. Mater.* **10**, 569 (2011).